Reduction of Atmospheric Effects on InSAR Observations Through Incorporation of GACOS and PCA Into Small Baseline Subset InSAR

Xuesong Zhang, Zhenhong Li, *Senior Member, IEEE*, and Zhenjiang Liu

***Abstract*— Small Baseline Subset InSAR (SBAS InSAR) utilizes a series of synthetic aperture radar (SAR) interferograms to generate a time series that can analyze the surface displacements of coherent points. Still, atmospheric errors in interferometric SAR (InSAR) measurements can seriously affect the reliability of the surface displacement time series. In this article, a new approach incorporating the Generic Atmospheric Correction Online Service for InSAR (GACOS) and principal component analysis (PCA) is proposed to reduce atmospheric errors in SBAS InSAR. Its application to Southern California, USA suggests that the incorporation of GACOS and PCA can efficiently reduce atmospheric effects on InSAR observations and hence improve the accuracy of InSAR-derived surface displacements. The overall standard deviations of the SAR interferograms were reduced from 4.97 to 2.02 rad after applying GACOS and PCA with the root mean square error (RMSE) reducing by 61.1% from 18 to 7 mm. In addition, comparisons between different PCA processing strategies suggest that the more principal components are removed, the smaller the standard deviations of the interferograms, but the lower the accuracy of InSAR-derived surface displacements.**

***Index Terms*— Atmospheric errors, Generic Atmospheric Correction Online Service for InSAR (GACOS), principal component analysis (PCA), Small Baseline Subset InSAR (SBAS InSAR), time series.**

I. Introduction

SMALL Baseline Subset InSAR (SBAS InSAR) can detect small surface displacements that occur on spatial scales of tens to hundreds of kilometers and time periods of several years or longer. SBAS InSAR has been widely used to monitor urban ground subsidence due to geological formations and human activity [1], [2], postseismic and interseismic deformation [3], [4], and ground deformation due to volcanic eruptions [5], [6].

The atmosphere is the main source of error for repeat-pass interferometric SAR (InSAR) because of the phase delay in radio signal propagation through the atmosphere (especially the part due to tropospheric water vapor). A 20% change in relative humidity in the troposphere may produce apparent displacements of >10 cm [7], [8]. Water vapor is mainly contained in the troposphere near the ground, where strong turbulent mixing processes occur; this part of the turbulent atmosphere is independent of topography and may be present in both flat and mountainous regions [9]. The turbulent atmosphere is associated in space on a scale of a few kilometers. In addition to the turbulent atmosphere, the stratified atmosphere has important impacts on InSAR observations. The stratified atmosphere produces topography-dependent range changes, and hence, topography-dependent atmospheric delays are often obvious in mountainous regions [10], [11].

The effects of the atmosphere can be mitigated using the statistical properties of the atmosphere in space or in time and space. Assuming the deformation rate is constant over the time, the signals that are uncorrelated in time can be reduced by stacking multiple independent interferograms, and hence, the accuracy of the deformation rate can be improved [12]. Under an identical assumption, Tymofyeyeva and Fialko [13] presented a common scene stacking approach to estimate atmospheric effects including both tropospheric and ionospheric delays through the averaging of redundant interferograms that share a common scene. Assuming that atmospheric signals are temporally uncorrelated and spatially correlated, atmospheric errors can be reduced using high-pass filtering in time and low-pass filtering in space [14]. Such approaches are effective to mitigate the effects of the turbulent atmosphere, but they may not work for the effects of the stratified atmosphere since it tends to be spatially correlated with the terrain and has some seasonal variation in time [15]. Several previous studies also proposed empirical models to reduce atmospheric effects by quantifying the relationship between atmospheric phase and terrain height [16].

The Global Navigation Satellite System (GNSS) or GNSS networks are effective tools for obtaining tropospheric delays and/or atmospheric water vapor content [17], [18]. The interpolation of the precipitable water vapor (PWV) obtained from

Manuscript received 8 July 2022; revised 15 January 2023; accepted 28 May 2023. Date of publication 1 June 2023; date of current version 14 June 2023. This work was supported in part by the National Natural Science Foundation of China under Grant 41941019; in part by the Shaanxi Province Science and Technology Innovation Team under Grant 2021TD-51; in part by the Shaanxi Province Geoscience Big Data and Geohazard Prevention Innovation Team (2022); and in part by the Fundamental Research Funds for the Central Universities, Chang'an University (CHD), under Grant 300102260301, Grant 300102261108, and Grant 300102262902. *(Corresponding author: Zhenhong Li.)*

Xuesong Zhang is with the College of Geological Engineering and Geomatics, Chang'an University, Xi'an 710054, China, and also with the Big Data Center for Geosciences and Satellites (BDCGS), Xi'an 710054, China (e-mail: xuesong.zhang@chd.edu.cn).

Zhenhong Li is with the College of Geological Engineering and Geomatics, Chang'an University, Xi'an 710054, China, also with the Key Laboratory of Loess, Xi'an 710054, China, and also with the Key Laboratory of Western China's Mineral Resource and Geological Engineering, Ministry of Education, Xi'an 710054, China (e-mail: zhenhong.li@chd.edu.cn).

Zhenjiang Liu is with the College of Geological Engineering and Geomatics, Chang'an University, Xi'an 710054, China, and also with the Big Data Center for Geosciences and Satellites (BDCGS), Xi'an 710054, China (e-mail: zhenjiang.liu@chd.edu.cn).

Digital Object Identifier 10.1109/TGRS.2023.3281783

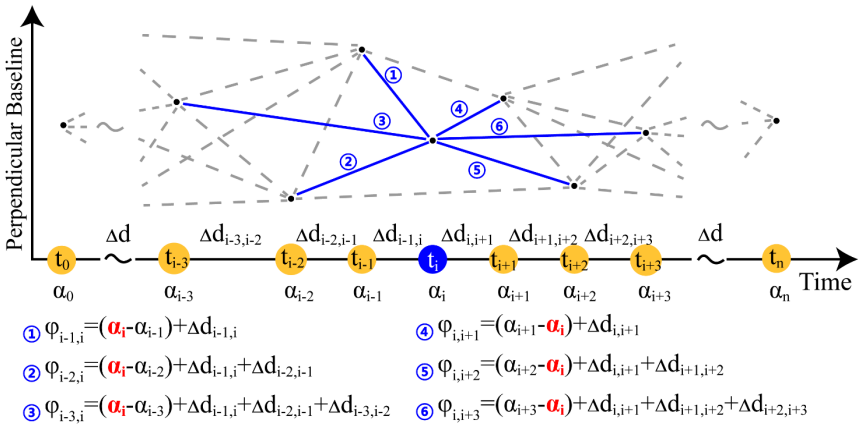

Fig. 1. SAR interferograms in a subnetwork. Black dots represent SAR acquisitions, and blue solid and gray dashed lines and connecting dots represent SAR interferograms. The blue lines represent the interferograms in this subnetwork, while the gray lines represent those excluded in this subnetwork. Note that α_i represents atmospheric effects on the SAR image acquired at time t_i, $\Delta d_{i(i+1)}$ indicates the LOS surface displacement occurring during the period of $[t_i, t_{i+1}]$, and φ_{ij} represents the interferometric phase between two acquisition times t_i and t_j.

GNSS networks can be used to obtain atmospheric water vapor distribution over a certain region, which can be applied to correct atmospheric errors in SAR interferograms [19], [20], [21]. However, the performance is easily affected by the limited spatial resolution of the GNSS network, and the variation between different interpolation algorithms can also cause different correction effects [22], [23], [24]. Space-based near-infrared (NIR) water-vapor products [e.g., the NASA Moderate Resolution Imaging Spectroradiometer (MODIS) and the ESA Medium Resolution Imaging Spectrometer (MERIS)], which can capture water vapor over wide areas, have been shown the potential to reduce atmospheric delays in interferograms [20], [25], [26], [27]. MERIS was carried on the ENVISAT satellite and imaged alongside Advanced Synthetic Aperture Radar (ASAR), with higher resolution than MODIS, providing an opportunity to precisely reduce atmospheric effects on ASAR measurements [26], [28]. However, MODIS and MERIS are sensitive to the presence of clouds, and they can only be employed to reduce atmospheric effects on InSAR measurements under clear-sky conditions, which limit their applications. In addition, numerical simulation models can simulate water vapor at medium and large scales.

Numerical simulation models, which simulate meteorological data with continuous temporal resolution and spatial resolution of several tens of kilometers, have been successfully applied to the atmospheric correction of SAR interferograms (e.g., [29], [30], [31]). Coarse spatial resolution, regional differences, seasonal errors, and responses to extreme weather are the problems and challenges of the numerical simulation model in the atmospheric errors correction of InSAR [32]. In addition, the performance of numerical simulation models varies from place to place; for example, some global weather models have high accuracy in Europe, while there are large errors in some parts of Asia (especially southwest China), which may be due to the different data sources in different regions. Generic Atmospheric Correction Online Service for InSAR (GACOS) uses the iterative tropospheric decomposition (ITD) model to estimate the stratified and turbulent atmospheric delays, respectively [33]; it utilizes high-resolution European Centre for Medium-Range Weather Forecasts (HRES ECMWF) data, GNSS tropospheric delays, and global digital elevation model (DEM) datasets, providing a globally available near real-time atmospheric correction product [34], [35]. GACOS has proven to be an effective InSAR atmospheric correction method for reducing medium-to-long-wavelength atmospheric effects as well as topography-dependent atmospheric signals [34], [35], [36], [37], [38]. Although GACOS has absorbed some of the GNSS tropospheric delays, the atmosphere at small scales (e.g., 100 m to a few kilometers) remains difficult to estimate and mitigate effectively due to the limited density of stations in the GNSS network used [39]. Since the main data for GACOS come from the numerical simulation model, HRES ECMWF, they also inherit some common disadvantages of numerical simulation models, such as limited spatiotemporal resolutions and seasonal errors. Therefore, residual atmospheric errors may remain after GACOS correction and further corrections are required.

For SBAS InSAR, SAR images with small temporal and spatial baselines are interferometrically processed to generate interferograms. Here, we refer to all the interferograms obtained from one identical SAR image as a subnetwork (see Fig. 1). With a common SAR image, specific atmospheric errors shall always exhibit in all the interferograms derived from the subnetwork. The interferograms in the subnetwork share a common SAR image, and hence, they have similar image characteristics (i.e., they have similar atmospheric errors).

Principal components analysis (PCA) is often used to reduce the dimensionality of a set of data and plays an essential role in target recognition, detection, and classification [40], [41], [42]. PCA processing on a set of data can usually actualize multiple principal components. The component with the greatest variance is the first principal component, which contains the most important features in the data, while the final principal component is often noise [43]. Therefore, PCA

can be used to identify features in images or remove noise. The main advantages of the PCA algorithm are: 1) only the variance is used to measure the amount of information, and it is not affected by factors other than the dataset; 2) the principal components are orthogonal, which can eliminate the factors that affect the original data components; and 3) the main operation of the computation is the eigenvalue decomposition or singular value decomposition (SVD), which is easy to implement.

Since GACOS cannot completely eliminate atmospheric errors, there will be residual atmospheric errors in the subnetwork. Note that residual atmospheric errors in the GACOS-corrected interferograms could be noteworthy and hinder the effectiveness of the GACOS correction [34]. We attempt to integrate the subnetwork concept with the PCA method to reduce the residual atmospheric errors in the GACOS-corrected interferograms and then provide a simple and efficient new algorithm for dealing with atmospheric errors in SBAS InSAR. In this article, the algorithm for reducing atmospheric errors is known as GACOS + PCA and consists of three steps: 1) to apply GACOS atmospheric correction to all original interferograms; 2) to use PCA to estimate and mitigate the residual atmospheric errors in the common SAR image of each subnetwork; and 3) to repeat step 2 until every subnetwork is done. The principles of SBAS InSAR, GACOS, and PCA methods are briefly described in Section II. The result is shown in Section III, and the conclusions are drawn in Section IV.

II. Methodology

A. SBAS InSAR

SBAS InSAR is a time-series InSAR method developed from coventional InSAR technology. Aiming to solve the problem of decorrelation and the inability to obtain a deformation time series using coventional InSAR technology, Berardino et al. [44] proposed the SBAS InSAR, which uses small baseline interferograms and SVD to obtain surface displacement time series. The method of multiple primary images is used to organize the network, and the SAR image pairs, with a small temporal baseline and spatial baseline, are used to form SAR interferograms. Due to the short revisit periods and excellent orbit control for global coverage achieved by the Sentinel-1A/B satellites, the small baseline requirement is inherently achieved. Then, according to the coherence in the interferograms, pixels with sufficient coherence are selected for 2-D [45] or 3-D [46] phase unwrapping. The phase can be inverted using SVD [44], least-square [47], or minimization of the L1-norm [48] to obtain the phase at the moment of SAR image acquisition (i.e., the phase variation with time). In addition, with SBAS InSAR, bandpass filtering is typically used to mitigate atmospheric errors. Bandpass filtering is often useful in cases, where atmospheric errors are considered to be time uncorrelated, and it ignores the temporal correlation of the stratified atmosphere.

Pixels for which the phase decorrelates little over short time intervals are the targets of the SBAS method [8]. In many SBAS InSAR algorithms, the measurements of many adjacent resolution elements are summed to further reduce the decorrelation noise (e.g., [44], [47]) (known as multilooking); the signal in each element is enhanced and the noise is further mitigated as long as the signal does not vary significantly over the region of the multilooking elements. Nevertheless, in extreme decorrelation situations, such as those in relation to scatterer motion or where coherent pixels are surrounded by decoherent pixels, multilooking operation may fail or reduce the signal-to-noise ratio (SNR). It should be pointed out that some low-amplitude, long-wavelength deformation signals (e.g., interseismic strain accumulation signals) may be mixed with the phase ramps caused by the uncertainties in SAR satellite orbits, so the measurements of such signals usually require a combination of SBAS InSAR and GNSS data [49], [50].

The use of interferograms with small baselines can ensure that most ground objects have sufficient coherence during the process, which can effectively avoid the effects of spatiotemporal decorrelation and enable the obtaining of denser coherent points in rural areas. However, it cannot completely avoid decorrelation because there are various sources contributing to decorrelation, including thermal noise, lack of parallelism between orbits at different acquisitions, spatial baseline noise, and surficial change [51]. The final precision of SBAS inversion depends on the number of SAR images, the selection of the threshold of coherence, and the approach to separate surface displacements from other signals.

B. GACOS

Yu et al. [52] developed the ITD model to separate the stratified and turbulent atmospheric delays [33]. The effects produced by the turbulent atmosphere are considered to obey inverse distance weighting, and the effects produced by the stratified atmosphere follow an exponential distribution. Using HRES ECMWF data, GNSS tropospheric delays, and global DEM datasets, an atmospheric correction product can be generated [35]. Due to the use of nonoptical data, GACOS can be independent of observational conditions, such as time or cloudiness, and hence can provide atmospheric correction maps at any moment in time globally.

In general, ITD can well reconstruct the medium-to-long-wavelength tropospheric delays as well as topography-dependent tropospheric delays, but short-wavelength topography-independent delays require a denser GNSS network (e.g., [39]). ECMWF tropospheric products are limited by the resolution of assimilation data and, even if they operate in a nested fashion, their products are subject to uncertainties. A recent study reported that the global standard deviations of the zenith tropospheric delay differences between HRES ECMWF and GPS were 1.54 cm [53].

C. PCA and Its Application to InSAR

Developed by Hotelling [54], PCA transfers a set of variables to a new coordinate system to obtain a new set of variables through a linear transformation. The individual variables in the new set are uncorrelated. The maximum variance of any projection of the original data is on the first coordinate system, and the second maximum variance is on the second coordinate

system [43]. The basic principle of PCA is to extract the information with the greatest variances in the variables. Mathematically, the direct measure of variability between data is the variance. Therefore, the requirements of PCA are satisfied if the variance between the same characteristic dimension from which all variables are extracted is maximized.

In PCA processing, SVD is often employed to carry out matrix decomposition. Eigenvalue decomposition is not used here because it is only applicable to square matrices, which are rarely encountered in practice. Assuming a matrix A of m rows and n columns, we can define the result of SVD decomposition of the matrix A as

$$A = U\Sigma V^{\mathrm{T}} \tag{1}$$

where U is a matrix of $m \times m$, Σ is a diagonal matrix of $m \times n$, and V is a matrix of $n \times n$. Each element on the main diagonal of Σ is a singular value. Each singular value represents the proportion of this principal component to the overall features [55]. Typically, the singular values are ordered from largest to smallest, and accordingly, the other two matrices are ordered; the higher the singular value, the more distinct the feature represented. Thus, the eigenvalues of the first few represent most of the characteristics of the original matrix.

PCA is used to obtain significant features in a set of data. As the interferometric phase of each pixel in an interferogram can be considered as the sum of various sources of error and deformation, PCA can be used for InSAR data. The interferometric phase φ_{ij} between two acquisition times t_i and t_j can be expressed as follows:

$$\varphi_{ij} = \Delta d_{ij} + \alpha_j - \alpha_i + \varphi_{\text{noise}} \tag{2}$$

where Δd_{ij} is the phase change in the radar line of sight (LOS) due to surface deformation occurring during the period from t_i to t_j and can be the sum of a series of adjacent $\Delta d_{i(i+1)}$. α_i and α_j represent the atmospheric contributions at times t_i and t_j, respectively. φ_{noise} is the error due to a range of factors, such as thermal noise, temporal decorrelation, incorrect digital elevation model, and the uncertainties in satellite orbits, and can often be neglected. Therefore, (2) can be simplified as follows:

$$\varphi_{ij} = \left(\alpha_j - \alpha_i\right) + \Delta d_{ij}. \tag{3}$$

As shown in Fig. 1, there are six SAR interferograms in the subnetwork, and for each coherent pixel, there should be six observation equations. It is clear that there are a range of variables (i.e., α and Δd) in the six observation equations, but the atmospheric phase of the common SAR image (i.e., α_i is the only variable exhibiting in each observation equation), suggesting that α_i shall account for the common features derived from all the SAR interferograms in the subnetwork using PCA. Note that PCA does not require equal time intervals between SAR acquisitions.

D. Incorporation of GACOS + PCA Into SBAS InSAR

Fig. 2(a) shows the workflow of GACOS + PCA including the detailed procedure of PCA under the subnetwork concept. All single look complex (SLC) images are co-registered to the same common primary image. Here, multilooking operation is used to suppress noise. Combined with precision orbit data, the co-registered SAR images with small baselines are interferometrically processed to generate SAR interferograms. Using an external DEM, the flat earth and topographic phases are removed from the original interferograms. Using a 2-D phase unwrapping method such as SNAPHU [56], the phase in the original interferograms can be unwrapped and the original unwrapped interferograms are obtained.

GACOS zenith tropospheric delay products are obtained through the GACOS website (http://www.GACOS.net) and then projected into the radar LOS with the incident angle being calculated pixel by pixel to obtain GACOS atmospheric correction maps. Finally, the GACOS atmospheric correction maps are applied to the original unwrapped interferograms to obtain the GACOS-corrected interferograms.

After GACOS correction, PCA is implemented subnetwork by subnetwork to determine the residual atmospheric signals of the common SAR image in each subnetwork [see Fig. 2(b)]. An interferogram can be considered a 2-D matrix with a rows and b columns. Each interferogram is converted from a 2-D image to a 1-D column vector. Let $n = a \times b$ and suppose that there are m interferograms in a subnetwork, and then, all the column vectors are combined into a matrix to obtain a 2-D matrix of $n \times m$. Substitute into matrix A in (1), and use SVD to obtain matrices $U_{m\times m}$, $\Sigma_{m\times n}$, and $V^{\mathrm{T}}_{n\times n}$. For noise reduction, traditional PCA keeps the first few principal components in order to retain most of the features, while the residual atmospheric error is the main feature in the subnetwork, which is the part we wish to discard. Therefore, in order to estimate and mitigate the residual atmospheric error, the first k principal components in PCA need to be deleted. After SVD, the first k items are removed, the last $m - k$ columns of the matrix $U_{m\times m}$ are retained, the last $(m-k)\times(n-k)$ submatrices of the matrix $\Sigma_{m\times n}$ are retained, and the last $n-k$ rows of the matrix $V^{\mathrm{T}}_{n\times n}$ are retained. Then, (1) is used to restore $U_{m\times(m-k)}$, $\Sigma_{(m-k)\times(n-k)}$, and $V^{\mathrm{T}}_{n\times(n-k)}$ to matrix A'. At this point, the first k principal components of the original matrix A have been removed, and the m corrected interferograms are obtained by the inverse operation from images to vectors [57].

Finally, the corrected interferograms are input into the standard SBAS InSAR, and the deformation rate and time series are obtained using the weighted least squares.

By removing the first one or two principal components after SVD decomposition, most of the common image features in the interferograms are removed. If too many principal components are removed, the signal of interest (e.g., deformation) is likely be removed as well and this is discussed later. Furthermore, due to the specific nature of the SVD algorithm, the proportion of each singular value to the sum of all the singular values cannot be accurately determined. As such, there is no precise control over which features to remove.

III. Application to Sentinel-1 Data Over Southern CA

Southern California is located in the west coast of the USA, and the Plate Boundary Observatory (PBO) has been

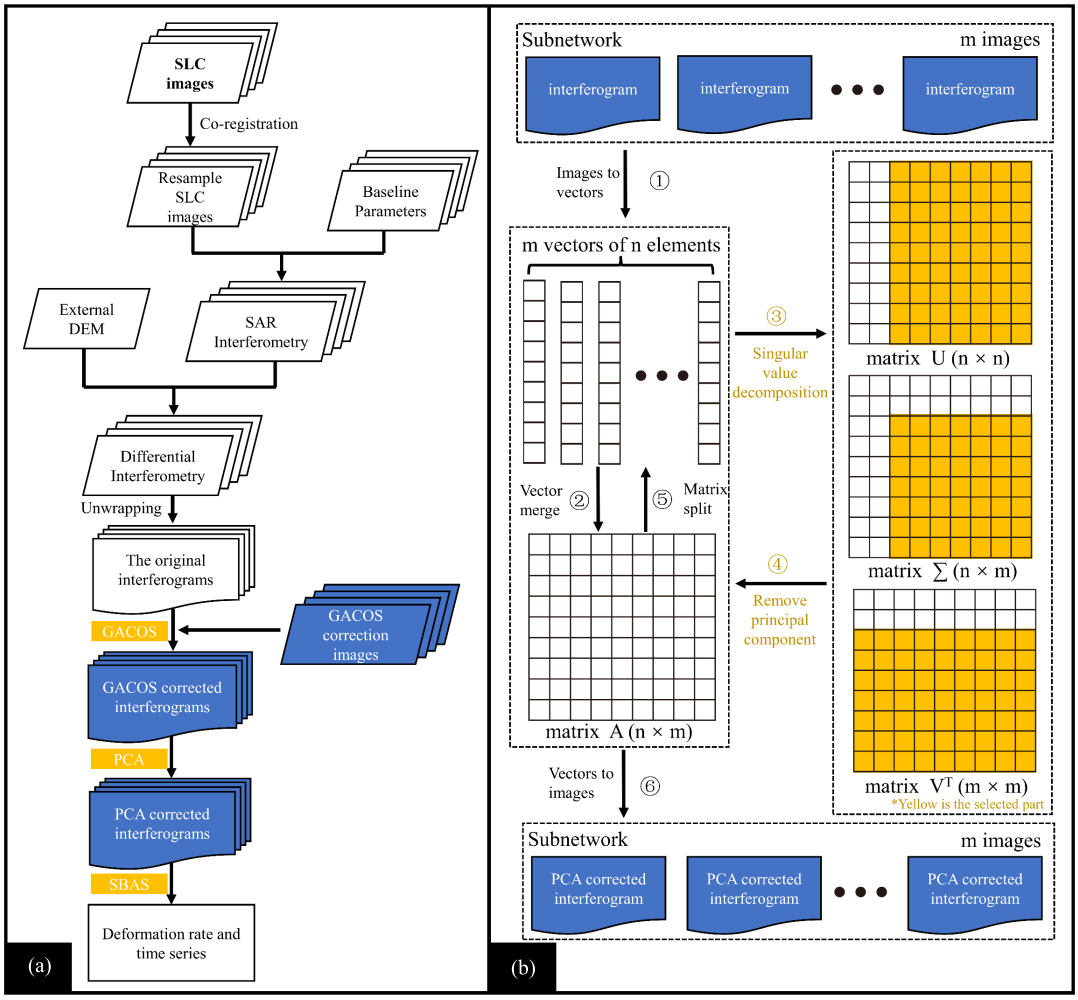

Fig. 2. Workflow of (a) GACOS + PCA and (b) PCA.

developed to measure the changes in the Earth's surface utilizing a variety of technologies and approaches, including GNSS stations, laser strainmeters, accelerometers, and geodetic imaging. PBO provides long time series of point deformation data from which to study plate motion, earthquakes, ground subsidence, and so on (e.g., [58], [59]), as well as sufficient data for comparing InSAR time-series results with GNSS time-series results. With its rich variety of terrain, southern California represents a valuable experimental area for InSAR algorithms.

A total of 127 Sentinel-1A/B descending SAR images were collected during the period from June 8, 2017 to June 5, 2021, with track 71 frame 479 (see Fig. 3) and a minimum time baseline of six days. The data utilized are interferometric wide (IW) strip mode data obtained by Terrain Observation by Progressive Scans (TOPS), with a range resolution of approximately 5 m and an azimuth resolution of approximately 20 m. The maximum time baseline was set to 100 days and eventually 741 interferograms were generated (see Fig. 4).

SAR images were processed according to the workflow in Fig. 2. The entire process of interfering was executed using the commercial software, GAMMA [60]. First, the SLC images were co-registered to the common primary image

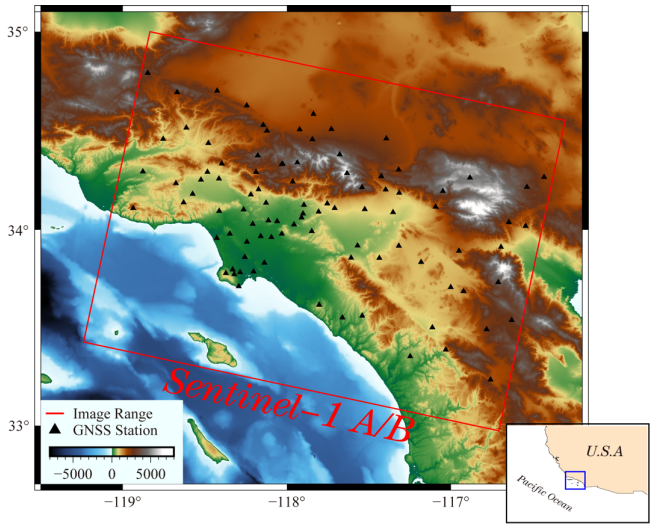

Fig. 3. Study area in southern California. Note that the red box indicates the coverage of Sentinel-1A/B Track 71, Frame 479, and the black triangles represent GNSS stations.

(acquired on August 15, 2019 during the middle of the entire time series). Once all images were co-registered, the ISP module was used for the interference process, using the

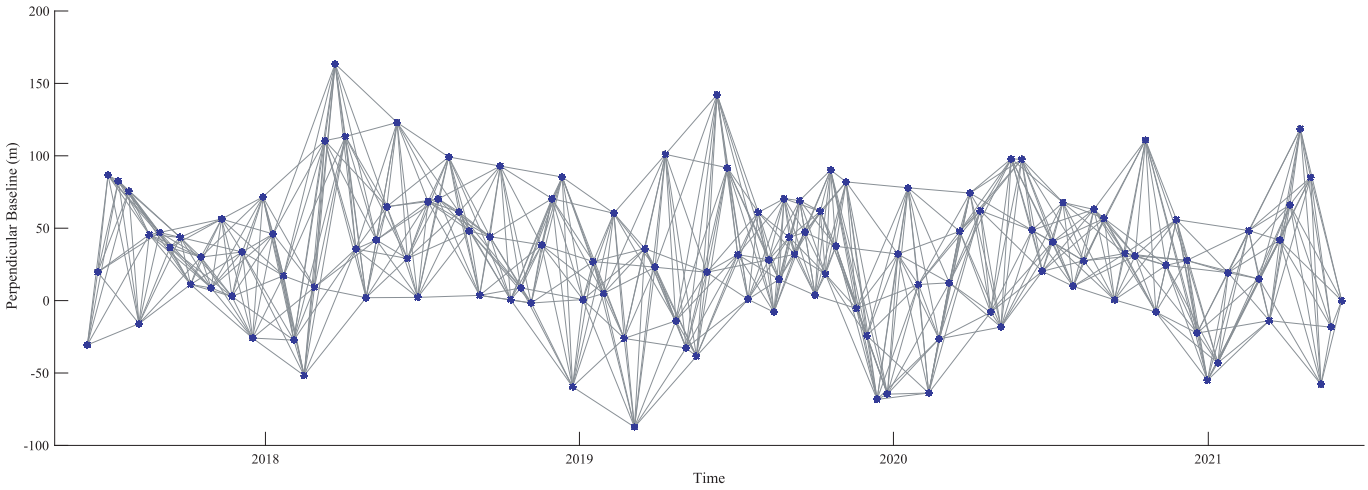

Fig. 4. Temporal and spatial baselines of the Sentinel-1A/B 741 interferograms.

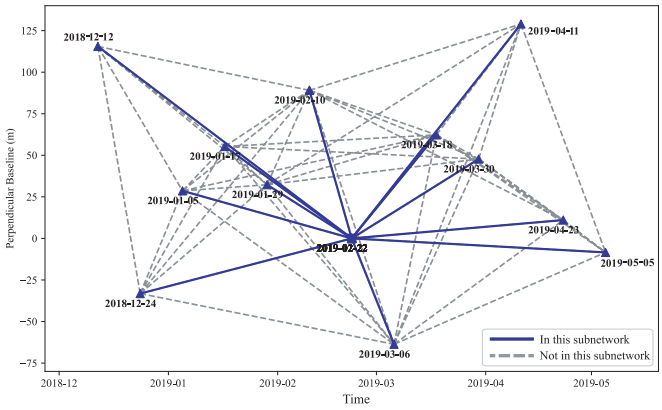

Fig. 5. Composition of a subnetwork (February 22, 2019, as an example). The blue lines represent the interferograms in this subnetwork, and the gray lines represent interferograms that are excluded in this subnetwork.

SRTM DEM as an external DEM to remove the flat and topographic effects. A 2-pixel multilooking operation in the range direction and a 10-pixel multilooking operation in the azimuth direction were performed to suppress noise. After generating the interferograms, the minimum cost flow (MCF) algorithm based on Delaunay triangulation [61], [62] was used for phase unwrapping to form the original interferograms. GACOS was employed to generate 127 atmospheric correction maps, and atmospheric corrections were applied to all the interferograms. Manual inspection of GACOS-corrected interferograms showed that medium-to-long-wavelength and topography-dependent atmospheric errors were significantly mitigated.

After selecting pixels with coherence greater than 0.6 as the coherent points, the entire SBAS network was reassembled into 127 subnetworks, with approximately 6–12 interferograms in each subnetwork. PCA was performed on each subnetwork to estimate the first principal component of each interferogram, and then, the residual atmospheric signals of the common SAR image were determined. Fig. 5 shows the subnetwork generated on February 22, 2019. Among the 12 interferograms in this subnetwork, the SAR image acquired on February 22, 2019 was considered as the primary (i.e., common) image and the remainders as the secondary images; those in the subnetwork are all shown as solid blue lines and the gray dashed lines represent interferograms excluded in this subnetwork. Finally, the inversion of the time series was performed.

A. Comparison Between Interferograms

In accordance with the processing flow designed above, the interferograms were processed using GACOS and GACOS + PCA, respectively. Among the 741 interferograms generated, the 11 interferograms with the time baseline of six days were selected for display in Fig. 6. The minimum revisit interval for Sentinel-1 satellites is six days, and unless a sudden geological event (such as an earthquake or landslide) causes ground deformation during such a short period, there should be no obvious deformation signal in the 6-day interferograms. A search of the U.S. Geological Survey earthquake catalog website (https://www.earthquake.usgs.gov/earthquakes/search/) shows no earthquake of magnitude 4.5 or greater in the area during the study period. Therefore, it is assumed in this article that all the 6-day interferograms are in principle free of surface deformation and can be used to evaluate the performance of atmospheric correction. The phase variations that appear in the 6-day interferograms are considered to be the effect of atmospheric errors.

In Fig. 6, the first row shows the original unwrapped interferograms; obvious errors in all the 11 interferograms and some medium-to-long-wavelength errors can be seen. The second row sets out the corrected interferograms after the GACOS correction. Most of the errors, especially those medium-to-long-wavelength errors and topography-dependent errors, were reduced; however, there remained residual atmospheric errors in some interferograms. The third row shows the interferograms after the GACOS + PCA correction, where most atmospheric errors were estimated and reduced, except for some short-wavelength errors.

Fig. 7 shows the six interferograms in the subnetwork with the SAR image of July 9, 2018 as the primary (i.e., common)

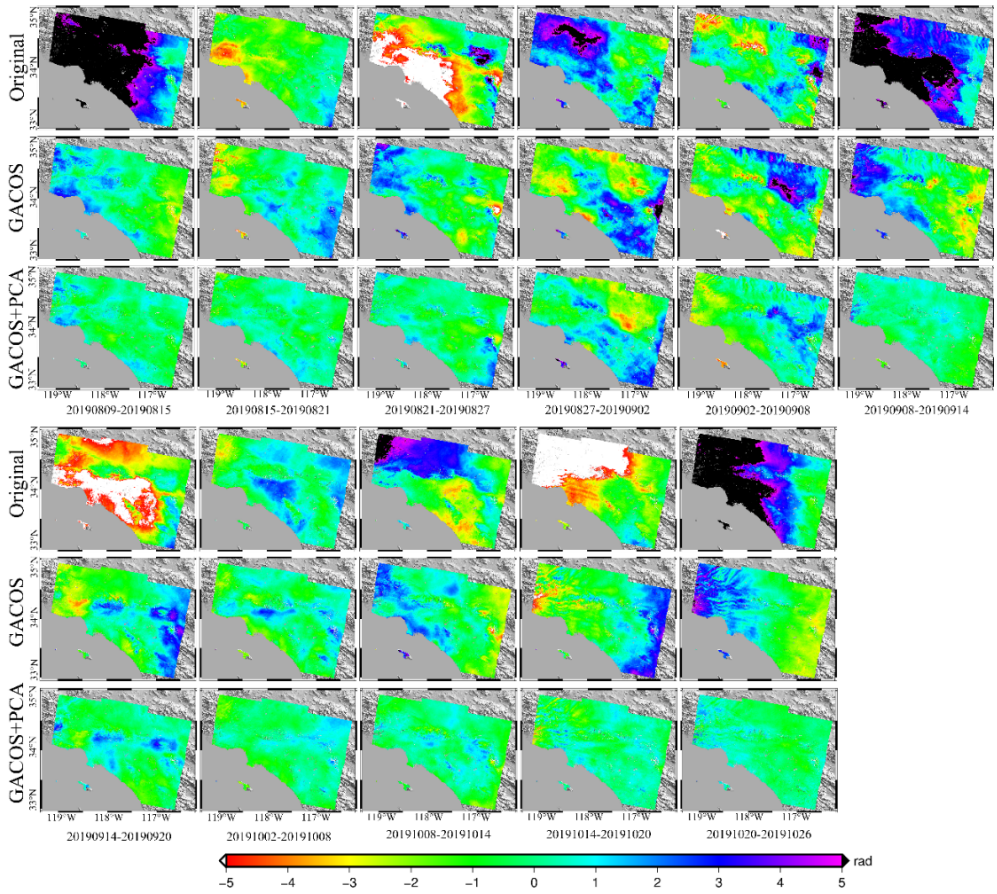

Fig. 6. Interferograms are formed using the 6-day time interval. The first row shows the original unwrapped interferograms, the second row shows the corrected interferograms after the GACOS correction, and the third row shows the interferograms corrected by the GACOS + PCA.

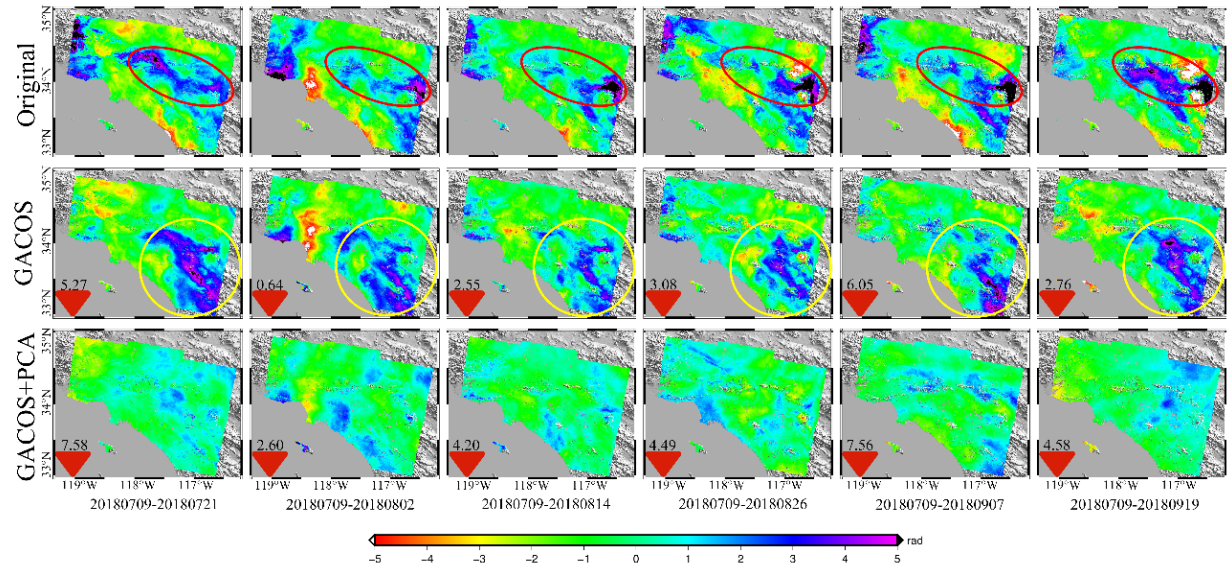

Fig. 7. Interferograms in the subnetwork with the SAR image of July 9, 2018 as the primary (i.e., common) image. The first row shows the original interferograms, the second row shows the corrected interferograms after the GACOS correction, and the third row shows the corrected interferograms after the GACOS + PCA correction. The red and yellow circles indicate the atmospheric errors. The numbers on the red arrows indicate the reduced values (unit: rad) of the standard deviations compared with the original interferograms.

image. Some similar patterns are evident in both the original interferograms and the GACOS-corrected interferograms, as shown in the red and yellow circles in the figures. Such similar patterns are mostly a result of the atmospheric effects from the July 9, 2018 image with additional contributions from the secondary images. The numbers on the red arrows

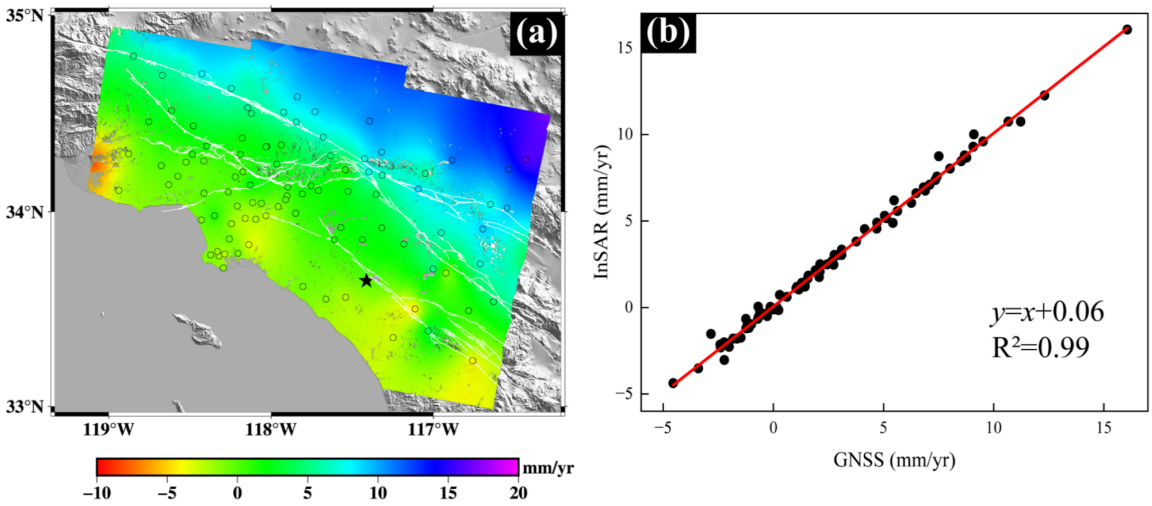

Fig. 8. (a) Deformation velocity map derived from GNSS and InSAR. (b) Correlation between GNSS and InSAR mean velocities of GNSS stations. Note that: 1) the black pentagram shows the reference area of the InSAR deformation velocity map; 2) black circles represent the GNSS stations; and 3) white lines represent active faults from USGS (https://www.usgs.gov/natural-hazards/earthquake-hazards/faults).

TABLE I
STANDARD DEVIATIONS OF 741 INTERFEROGRAMS

Method	Standard deviation of interferograms (rad)		
	Minimum	Maximum	Average
Original interferograms	1.09	11.11	4.97
GACOS	1.02	6.51	3
GACOS+PCA	0.84	4.51	2.02

represent the reduction in the standard deviation of the interferogram compared with the original interferogram after the GACOS and GACOS + PCA corrections, respectively. Following the GACOS correction, the standard deviations of the interferograms were reduced by 0.64–6.05 rad compared with the original interferograms. After the GACOS + PCA correction, the standard deviations of the interferograms were reduced by 2.60–7.58 rad than the original interferograms. The most considerable reduction was the interferogram with the smallest interval, 20180709–20180721, with a decrease of 77.9%. The interferogram with the least reduction was 20180709–20180202, reduced by 51.7%.

The standard deviations of the original interferograms and the interferograms corrected using the GACOS and GACOS + PCA were calculated and are shown in Table I. Overall, the standard deviations of the interferograms obtained using the GACOS + PCA were 59.4% less than the original interferograms and 32.7% less than the standard deviations of the GACOS-corrected interferograms. For the most interferograms, the reduction in the standard deviations of the GACOS + PCA corrected interferograms compared with the original ones ranged from 30.7% to 74.9%. Among the 741 interferograms, there exist six interferograms with increased standard deviations after the GACOS + PCA correction compared with those after the GACOS correction: 202200211–20200411 (60), 20170924–20171123 (60), 20200223–20200505 (72), 20210301–20210418 (48), 20210301–20210430 (60), and 20180428–20180510 (12). These six interferograms had a minimum time interval of 12 days and a maximum of 72 days. All the six also had smaller standard deviations after the GACOS correction than the original interferograms.

B. Evaluation of the GACOS + PCA Using GNSS Data

The standard deviation of the unwrapped phase is only representative of the overall noise level of the whole interferogram [36] and does not necessarily reflect the actual accuracy of InSAR derived surface displacements. Hence, the linear deformation velocity and time-series data from the widely distributed GNSS stations were used to assess the performance of the GACOS + PCA on InSAR.

GNSS-derived velocities and daily positions from the PBO network were downloaded from USGS (https://earthquake.usgs.gov/monitoring/gps) [63]. Fig. 8(a) shows the deformation velocity map derived from the integration of GNSS and InSAR observations. Considering the fact that Greater Los Angeles and its surrounding region experience complicated surface deformation patterns due to tectonic and nontectonic processes (e.g., [64], [65]), the comparisons of deformation from InSAR and GNSS observations should be performed through the mapping of GNSS-derived 3-D surface displacements (and/or surface displacement velocities) into the satellite LOS (e.g., [20], [66]).

Ninety-four GNSS stations within the Sentinel-1A/B coverage were selected to assess the performance of the GACOS + PCA on the SBAS InSAR time series. Comparisons were made with the time series of points obtained from the original interferograms, GACOS-corrected interferograms, and GACOS + PCA corrected interferograms. It is essential to note that the unwrapped phase (unit: rad) in all the interferograms was converted into the surface displacements (unit: mm) in the radar LOS, with negative values implying the Earth's surface was moving away from the satellite.

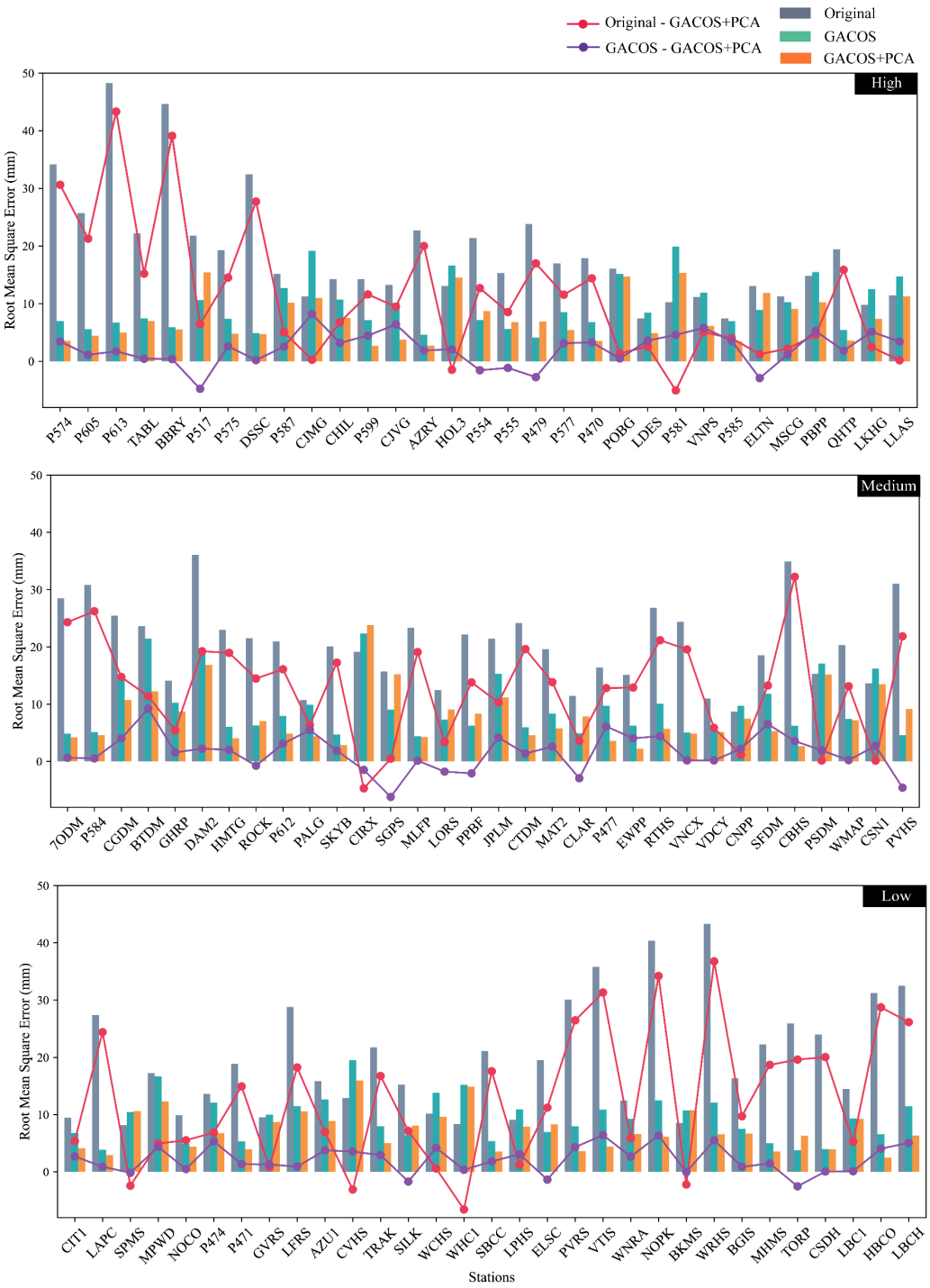

Fig. 9. RMSEs of the differences between GNSS LOS displacement time series and those from the original interferograms (gray), GACOS (green), and GACOS + PCA (orange), sorted by station altitudes and divided into high, medium, and low altitude. The red lines are the RMSE of the original interferogram minus the RMSE of GACOS + PCA and the purple lines indicate the RMSE of GACOS minus the RMSE of GACOS + PCA.

Fig. 9 shows the root mean square error (RMSE) of the differences between GNSS LOS displacement time series and those obtained by the original interferograms, GACOS, and GACOS + PCA. Among the 94 selected GNSS stations, 87 of those using GACOS + PCA obtained a smaller RMSE than the original interferograms, and 73 GNSS stations using GACOS + PCA obtained the smallest RMSE of the three methods. The most significant improvement to the original interferograms occurred at station P613, where the RMSE decreased from 48 mm in the original interferograms to 5 mm after GACOS + PCA. The greatest improvement in the GACOS results after the PCA correction was station BTDM, where the RMSE reduced from 21 to 12 mm. The RMSE between the GNSS-derived displacements in the LOS direction and those from GACOS + PCA, GACOS, and the original interferograms are 7, 11, and 18 mm, respectively.

TABLE II
GNSS STATION CLASSIFICATION IN TERMS OF ELEVATION

Altitude	< 200 m	> 200 m and < 800 m	> 800 m
Class	Low	Medium	High
Number	31	32	31

GACOS + PCA reduced the RMSE of GACOS and the original interferograms by 36.4% and 61.1%, respectively.

All the 94 GNSS stations can be divided into high-, medium-, and low-altitude stations according to their elevation, with the highest station being P574 (2874 m) and the lowest LBCH (−28 m). As shown in Table II, there are 31, 32, and 31 high-, medium-, and low-altitude stations, respectively, of which six stations below sea level are counted in the low-altitude stations. GACOS + PCA reduced the RMSE of the original interferogram by an average of 11 mm at high-altitude stations, 13 mm at medium-altitude stations, and 13 mm at low-altitude stations.

To further examine the impact of the attitude on the correction performance, all the GNSS stations are shown in three different categories according to their altitudes in Fig. 9, namely, high, medium, and low altitudes. Note that the red lines indicate the RMSE differences between the original interferograms and GACOS + PCA, the purple lines indicate the RMSE differences between GACOS and GACOS + PCA, and positive values indicate the improvement of GACOS + PCA against the former. Of the 31 GNSS stations at high altitude, 29 had a smaller RMSE after GACOS + PCA than the original interferograms and 26 stations had a smaller RMSE after GACOS + PCA than the GACOS. In the case of the HOL3, the RMSE increased from 13 mm in the original interferograms to 14 mm after GACOS + PCA correction; however, it is worth noting that, after the GACOS correction, it had an RMSE of 17 mm. PCA continued to play its part in correcting the GACOS result. For the GACOS results, PCA achieved good corrections in high-altitude stations, except for the P517 station, where the correction was poor, with an increase in RMSE of 5 mm after the PCA.

After the GACOS + PCA correction, 31 of the 32 stations at midaltitude had a smaller RMSE than the original interferograms and 25 had a smaller RMSE than GACOS. For the original interferograms, the best correction with GACOS + PCA was the CBHS station with a 32-mm reduction in the RMSE and the worst was the CIRX station with an increase of 5 mm. Among the seven stations where the RMSE of the GACOS + PCA increased compared to the GACOS correction, the seven stations only had an average increase in RMSE of 3 mm.

Of the 31 low-altitude GNSS stations, the RMSE was reduced after GACOS + PCA at 27 stations compared with the original interferograms and at 26 stations compared with GACOS. The station with the greatest reduction in RMSE was WRHS, with an RMSE of 43 mm for the original interferograms, 12 mm for the GACOS correction, and 6 mm for the GACOS + PCA correction. Another notable station was CVHS, where the RMSE of the original interferograms was 13 mm, after GACOS was 20 mm, and the GACOS + PCA result was 16 mm, with the PCA operation correcting some of the bias due to GACOS.

TABLE III
INFORMATION OF SELECTED GNSS STATIONS

Class	Station name	Longitude (°)	Latitude (°)	Altitude (m)
High	P574	-117.634	34.287	2873.769
	TABL	-117.678	34.382	2228.028
	P577	-117.319	34.305	999.538
	P585	-116.546	34.019	958.141
Medium	7ODM	-117.093	34.116	762.084
	P612	-117.316	34.187	531.715
	JPLM	-118.173	34.205	423.978
	EWPP	-117.526	34.104	330.470
Low	CIT1	-118.127	34.137	215.351
	AZU1	-117.896	34.126	144.742
	PVRS	-118.321	33.774	59.829
	TORP	-118.331	33.798	-5.216

In general, GACOS + PCA achieved good correction results. At low-altitude stations, 83.9% of GNSS stations had a reduced RMSE after GACOS + PCA compared with GACOS; this percentages were 78.1% and 83.9% for medium- and high-altitude stations, respectively. Among the 17 stations where the RMSE of GACOS + PCA increased compared to GACOS, except for the SGPS station, which increased by 6 mm, the increase of the RMSE at other stations did not exceed 4 mm, and the average increase of the RMSE at the 17 stations was 2 mm.

Furthermore, within the different categories, four stations were selected based on altitude and the coherence of the GNSS data. Table III shows 12 selected GNSS stations, four stations for each category, and Fig. 10 shows their LOS surface displacements from GNSS, the interferograms after the GACOS correction, and those after the GACOS + PCA correction. GACOS + PCA shows better performance than GACOS at high, medium, and low altitudes, with closer agreements with the GNSS results (i.e., lower RMSE differences). Note that no significant difference can be observed between the results at high, medium, and low altitudes.

C. Results of Different PCA Processing Strategies

In this experiment, the first principal component in the subnetwork was removed following PCA, because we assumed that the residual atmospheric errors after the GACOS atmospheric correction were mainly concentrated here. However, in reality, it could not accurately be determined in which principal components, the atmospheric errors existed. The principal component weights obtained by SVD are not fixed, and hence, it is impossible to accurately determine which of the principal components contain the residual atmospheric errors. The proportions of the first five principal components of subnetworks are shown in Table IV. In all the subnetworks, the first principal component accounts for approximately 16.0%–39.4% of all the principal components, with an average of about 25.3%. The second principal component accounts for approximately 9.4%–21.2% of the total, with an average

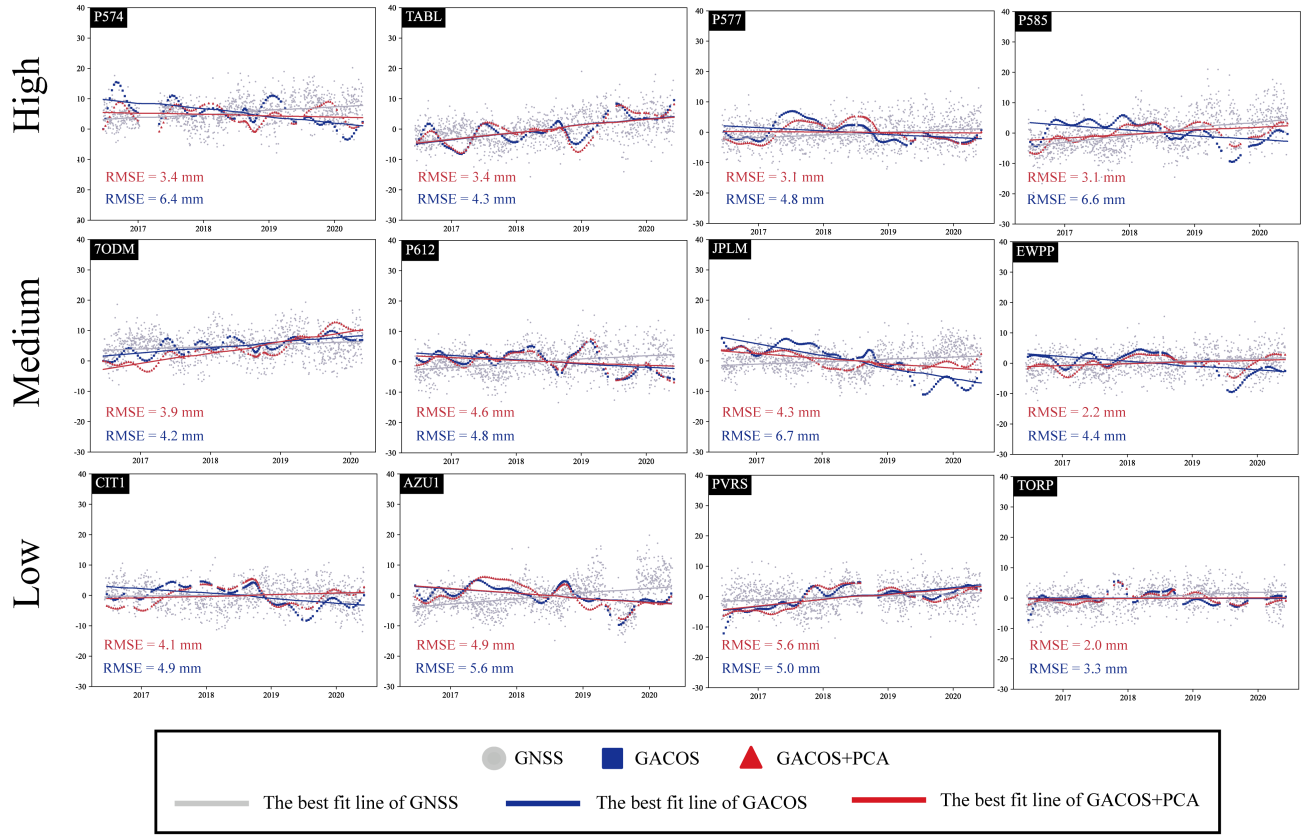

Fig. 10. LOS surface displacement time series from GNSS (gray points), the GACOS method (blue points), and the GACOS + PCA method (red points). In addition, the best-fit lines of GNSS (gray lines), GACOS (blue lines), and GACOS + PCA (red lines) are also drawn.

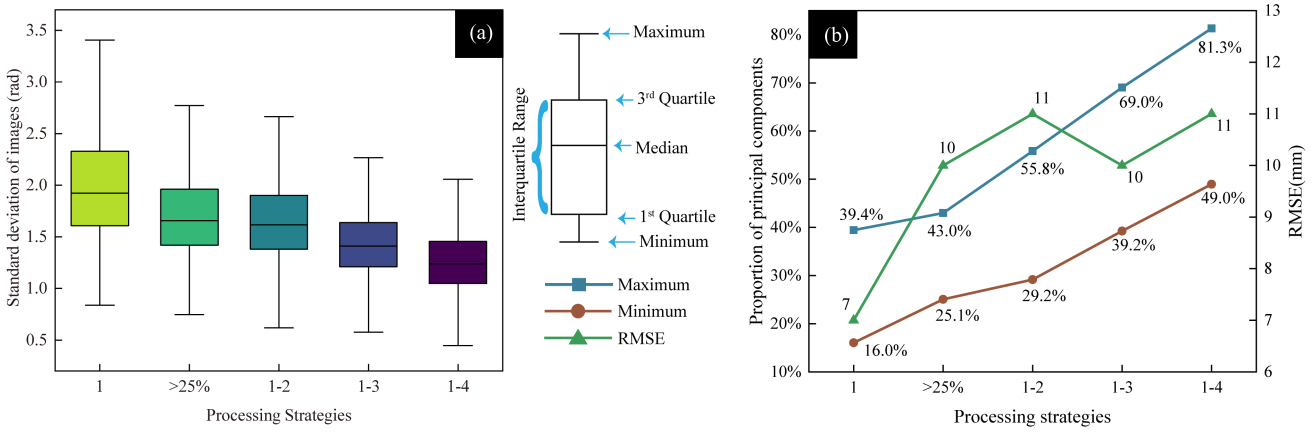

Fig. 11. (a) Standard deviations of the interferograms obtained from different processing strategies. (b) Range of proportions of different principal components in the total and the RMSE between the results of different strategies and GNSS deformation. Of the horizontal coordinates, "1," ">25%," "1–2," "1–3," and "1–4" represent the removal of the first principal component, the removal of at least 25% of the principal components and the removal of the first two, first three, and first four principal components, respectively.

of 13.9%. The proportion after the fifth principal component is small and not listed.

Two strategies of PCA for removing principal components were tested. In the first strategy, a sufficient proportion of the principal components was removed, where the first principal component was less than this proportion; the second principal component was removed until this proportion was satisfied. In this experiment, this proportion was set to 25%. The second strategy removed additional principal components; we tested the results of removing the first, the first two, the first three, and the first four principal components. In addition, the other processing steps were the same for both strategies.

Fig. 11(a) shows the standard deviations of the interferograms obtained from different processing strategies. Fig. 11(b)

TABLE IV
PROPORTION OF DIFFERENT PRINCIPAL COMPONENTS TO THE TOTAL

Principal Component	Ratio to overall		
	Average	Maximum	Minimum
1st	25.3%	39.4%	16.0%
2nd	13.9%	21.2%	9.4%
3rd	10.3%	15.0%	6.7%
4th	8.6%	14.1%	6.1%
5th	7.5%	11.0%	5.6%

presents the range of the ratio of principal components to all of the principal components selected by these two strategies and the RMSE between the GNSS displacements and the time series of the GACOS + PCA.

Undoubtedly, the higher the ranking of the principal component obtained from SVD, the more subnetwork features this principal component has, which is represented as a larger standard deviation in Fig. 11(a). So, the greater the number of principal components that are removed, the smaller the standard deviation of the interferogram will be. In Fig. 11(a), the average standard deviation of the 741 interferograms in the strategy with the first four principal components removed is 1.24 rad, which is 38.6% lower than the standard deviation of 2.02 rad with only the first principal component removed. However, the RMSE between the InSAR LOS surface displacement time series and GNSS displacements increases significantly with the standard deviations of the interferograms decreasing. Removing the first four principal components would remove between 49.0% and 81.3% of the principal components, and the RMSE would increase from 7 mm with only the first principal component removed to 11 mm.

The strategy that removed in excess of 25% of the principal components yielded an RSME of 10 mm, 42.9% higher than removing only the first principal component. This is sufficient to show that removing a greater number of principal components reduces the standard deviations of the interferograms, but reducing the accuracy of the InSAR measurements. This also means that removing too many principal components inevitably includes the deformation signal, and as the proportion of principal components removed increases, so does the amount of deformation removed. Therefore, we remove only the first principal component in order to remove as little deformation as possible.

D. Relationships Between the Correction Performance and Terrain Types

As shown in Fig. 3, the Sentinel-1 A/B IW image has a sufficiently large coverage area and contains a wide variety of terrain types, including flat land and mountainous terrain. In Fig. 12, the dots show the improvement in the RMSE of the GACOS + PCA over the original interferograms for the deformation from the GNSS. It can be seen that there is no significant difference in the magnitude of the improvement for different types of terrain, especially in some mountainous areas, where good correction performance can be observed. This is mainly due to the correction using the GACOS method

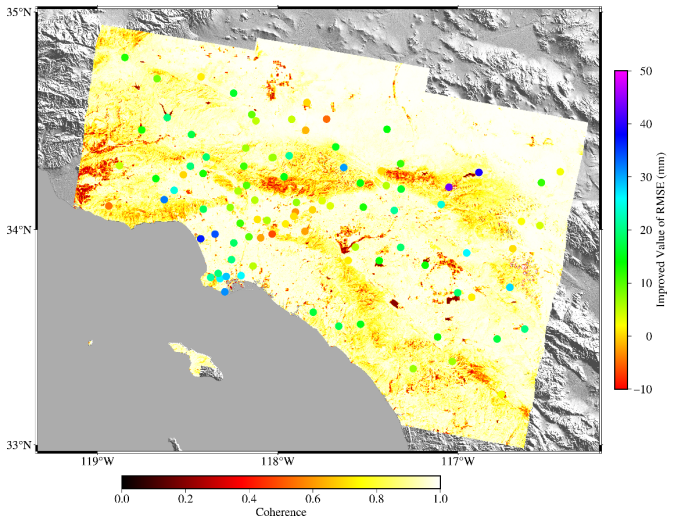

Fig. 12. Average coherence of interferograms and improved RMSE values for GACOS + PCA compared with the original interferograms. Positive values represent RMSE decreases.

prior to PCA processing, which effectively reduces terrain-related errors.

Fig. 12 also shows the average coherence of all interferograms. At the edges of the interferogram and in some areas where the coherence is poor, the improvement using GACOS + PCA is also significant. There may be unwrapping errors at the edges of the image, and in discontinuous regions, the reliability of the InSAR results is questionable in regions with low coherence. At the same time, in some mountainous areas, the coherence of the interferometric phase is low due to limitations in vegetation and imaging geometry. This low coherence reduces the reliability of the unwrapping phase, ultimately leading to larger errors in the time series compared with the GNSS displacements.

E. Application of GACOS

GACOS processing was used as a preprocessing step prior to PCA. GACOS correction was used to estimate and mitigate long-wave errors and terrain-related errors. Some experiments were carried out to determine whether it was possible to process the interferograms directly using PCA without GACOS correction. In areas with considerable topographic relief or valleys, processing interferograms using only PCA leaves more topography-related atmospheric errors and it is challenging to mitigate atmospheric errors by other means afterward. When detecting and identifying deformation, it is easy to locate these errors as areas of deformation, which leads to misjudgments and significantly affects the identification of deformation areas. In contrast, in areas with flat terrain, the absence of GACOS might not affect the effectiveness of atmospheric errors reduction (some extreme cases are not considered).

Therefore, we included GACOS processing in our processing flow. After using GACOS processing to remove most of the medium-to-long-wavelength and topography-dependent atmospheric errors, only the residual atmospheric errors are processed using the PCA method, avoiding the dispersal of

atmospheric errors into the remaining principal components. If some other external data or statistical methods are used to estimate the atmospheric errors, PCA can also correct the residual errors in their subnetworks.

IV. Conclusion and Future Work

This article presents a new technical framework of atmospheric correction for SBAS InSAR and GACOS + PCA, using PCA to estimate and mitigate atmospheric errors in a subnetwork consisting of GACOS-corrected interferograms. Between June 8, 2017 and June 5, 2021, a total of 127 Sentinel-1 A/B descending SAR images were used to generate 741 interferograms with atmospheric correction using GACOS and GACOS + PCA, respectively, and for SBAS InSAR to obtain a time series. The standard deviations of the interferograms with GACOS + PCA were reduced by 59.4% compared with the original interferograms and by 32.7% compared with the GACOS results. The RMSE obtained using GACOS + PCA processing at 87 of the 94 GNSS stations showed varying reductions in RMSE compared with the original interferograms.

Overall, the RMSE obtained using GACOS + PCA is improved by 61.1% compared with the original interferograms, 36.4% compared with GACOS. Using the PCA method combined with GACOS-corrected data improved the accuracy of the InSAR time series. In contrast, the GACOS + PCA method reduced accuracy after the GACOS processing in some areas but is still an improvement over the original interferograms. In addition, removing more principal components reduces the standard deviations of the interferograms but reduces the accuracy of the InSAR measurements. PCA can only find the component with the largest variance from the signal, which does not have much meaning, and based on the non-Gaussian characteristics of atmospheric errors, independent component analysis can better decompose atmospheric errors from InSAR interferograms, and using independent component analysis to estimate and mitigate atmospheric errors will be the next research focus.

Acknowledgment

The authors are grateful to the anonymous reviewers for their constructive comments and recommendations. Thanks to Chang'an University High Performance Computing Platform, European Space Agency (ESA) for the Sentinel-1 images, National Aeronautics and Space Administration (NASA), and National Mapping Authority (NIMA) for SRTM DEM.

References

[1] L. Hu et al., "Land subsidence in Beijing and its relationship with geological faults revealed by Sentinel-1 InSAR observations," *Int. J. Appl. Earth Observ. Geoinformation*, vol. 82, Oct. 2019, Art. no. 101886.

[2] E. Chaussard, S. Wdowinski, E. Cabral-Cano, and F. Amelung, "Land subsidence in central Mexico detected by ALOS InSAR time-series," *Remote Sens. Environ.*, vol. 140, pp. 94–106, Jan. 2014.

[3] Y. Wen, Z. Li, C. Xu, I. Ryder, and R. Bürgmann, "Postseismic motion after the 2001 MW7.8 Kokoxili earthquake in Tibet observed by InSAR time series," *J. Geophys. Res., Solid Earth*, vol. 117, Aug. 2012, Art. no. B08405.

[4] J. Biggs, T. Wright, Z. Lu, and B. Parsons, "Multi-interferogram method for measuring interseismic deformation: Denali Fault, Alaska," *Geophys. J. Int.*, vol. 170, no. 3, pp. 1165–1179, Sep. 2007.

[5] A. Babu and S. Kumar, "SBAS interferometric analysis for volcanic eruption of Hawaii island," *J. Volcanology Geothermal Res.*, vol. 370, pp. 31–50, Jan. 2019.

[6] J. Fernández et al., "Gravity-driven deformation of Tenerife measured by InSAR time series analysis," *Geophys. Res. Lett.*, vol. 36, no. 4, Feb. 2009.

[7] H. A. Zebker, P. A. Rosen, and S. Hensley, "Atmospheric effects in interferometric synthetic aperture radar surface deformation and topographic maps," *J. Geophys. Res., Solid Earth*, vol. 102, no. B4, pp. 7547–7563, Apr. 1997.

[8] A. Hooper, D. Bekaert, K. Spaans, and M. Arıkan, "Recent advances in SAR interferometry time series analysis for measuring crustal deformation," *Tectonophysics*, vols. 514–517, pp. 1–13, Jan. 2012.

[9] R. F. Hanssen, *Radar Interferometry: Data Interpretation and Error Analysis*. Boston, MA, USA: Kluwer Academic, 2001, pp. 197–226.

[10] Z. W. Li, X. L. Ding, C. Huang, G. Wadge, and D. W. Zheng, "Modeling of atmospheric effects on InSAR measurements by incorporating terrain elevation information," *J. Atmos. Solar-Terrestrial Phys.*, vol. 68, no. 11, pp. 1189–1194, Jul. 2006.

[11] Z. Li, E. J. Fielding, P. Cross, and J.-P. Müller, "Interferometric synthetic aperture radar atmospheric correction: GPS topography-dependent turbulence model," *J. Geophys. Res., Solid Earth*, vol. 111, Feb. 2006, Art. no. B02404.

[12] D. T. Sandwell and E. J. Price, "Phase gradient approach to stacking interferograms," *J. Geophys. Res., Solid Earth*, vol. 103, no. B12, pp. 30183–30204, Dec. 1998.

[13] E. Tymofyeyeva and Y. Fialko, "Mitigation of atmospheric phase delays in InSAR data, with application to the eastern California shear zone," *J. Geophys. Res., Solid Earth*, vol. 120, no. 8, pp. 5952–5963, Aug. 2015.

[14] A. Ferretti, C. Prati, and F. Rocca, "Permanent scatterers in SAR interferometry," *IEEE Trans. Geosci. Remote Sens.*, vol. 39, no. 1, pp. 8–20, Jan. 2001.

[15] J. Jung, D. Kim, and S. Park, "Correction of atmospheric phase screen in time series InSAR using WRF model for monitoring volcanic activities," *IEEE Trans. Geosci. Remote Sens.*, vol. 52, no. 5, pp. 2678–2689, May 2014.

[16] C. W. Wicks, "Magmatic activity beneath the quiescent three sisters volcanic center, central Oregon cascade range, USA," *Geophys. Res. Lett.*, vol. 29, no. 7, pp. 1–26, 2002.

[17] M. Bevis, S. Businger, T. A. Herring, C. Rocken, R. A. Anthes, and R. H. Ware, "GPS meteorology: Remote sensing of atmospheric water vapor using the global positioning system," *J. Geophys. Res.*, vol. 97, no. D14, pp. 15787–15801, Oct. 1992.

[18] Z. Li, "Comparison of precipitable water vapor derived from radiosonde, GPS, and moderate-resolution imaging spectroradiometer measurements," *J. Geophys. Res.*, vol. 108, no. D20, pp. 1–12, 2003.

[19] F. Onn and H. A. Zebker, "Correction for interferometric synthetic aperture radar atmospheric phase artifacts using time series of zenith wet delay observations from a GPS network," *J. Geophys. Res.*, vol. 111, no. B9, pp. 1–16, 2006.

[20] Z. Li, "Interferometric synthetic aperture radar (InSAR) atmospheric correction: GPS, moderate resolution imaging spectroradiometer (MODIS), and InSAR integration," *J. Geophys. Res.*, vol. 110, no. B3, p. 10, 2005.

[21] Z. W. Li, X. L. Ding, and G. X. Liu, "Modeling atmospheric effects on InSAR with meteorological and continuous GPS observations: Algorithms and some test results," *J. Atmos. Solar-Terrestrial Phys.*, vol. 66, no. 11, pp. 907–917, Jul. 2004.

[22] S. Williams, Y. Bock, and P. Fang, "Integrated satellite interferometry: Tropospheric noise, GPS estimates and implications for interferometric synthetic aperture radar products," *J. Geophys. Res., Solid Earth*, vol. 103, no. B11, pp. 27051–27067, Nov. 1998.

[23] P. W. Webley, R. M. Bingley, A. H. Dodson, G. Wadge, S. J. Waugh, and I. N. James, "Atmospheric water vapour correction to InSAR surface motion measurements on mountains: Results from a dense GPS network on Mount Etna," *Phys. Chem. Earth, Parts A/B/C*, vol. 27, nos. 4–5, pp. 363–370, Jan. 2002.

[24] V. Janssen, L. Ge, and C. Rizos, "Tropospheric corrections to SAR interferometry from GPS observations," *GPS Solutions*, vol. 8, no. 3, pp. 140–151, Sep. 2004.

[25] Z. Li, E. J. Fielding, P. Cross, and R. Preusker, "Advanced InSAR atmospheric correction: MERIS/MODIS combination and stacked water vapour models," *Int. J. Remote Sens.*, vol. 30, no. 13, pp. 3343–3363, Jul. 2009.

[26] Z. Li, E. J. Fielding, P. Cross, and J.-P. Müller, "Interferometric synthetic aperture radar atmospheric correction: Medium resolution imaging spectrometer and advanced synthetic aperture radar integration," *Geophys. Res. Lett.*, vol. 33, no. 6, p. 4, 2006.

[27] Z. W. Li et al., "Correcting atmospheric effects on InSAR with MERIS water vapour data and elevation-dependent interpolation model," *Geophys. J. Int.*, vol. 189, no. 2, pp. 898–910, May 2012.

[28] Z. Li, J. P. Müller, P. Cross, P. Albert, J. Fischer, and R. Bennartz, "Assessment of the potential of MERIS near-infrared water vapour products to correct ASAR interferometric measurements," *Int. J. Remote Sens.*, vol. 27, no. 2, pp. 349–365, Feb. 2007.

[29] J. Foster, B. Brooks, T. Cherubini, C. Shacat, S. Businger, and C. L. Werner, "Mitigating atmospheric noise for InSAR using a high resolution weather model," *Geophys. Res. Lett.*, vol. 33, no. 16, p. 5, 2006.

[30] M.-P. Doin, C. Lasserre, G. Peltzer, O. Cavalié, and C. Doubre, "Corrections of stratified tropospheric delays in SAR interferometry: Validation with global atmospheric models," *J. Appl. Geophysics*, vol. 69, no. 1, pp. 35–50, Sep. 2009.

[31] T. Fournier, M. E. Pritchard, and N. Finnegan, "Accounting for atmospheric delays in InSAR data in a search for long-wavelength deformation in South America," *IEEE Trans. Geosci. Remote Sens.*, vol. 49, no. 10, pp. 3856–3867, Oct. 2011.

[32] Q. Jiang et al., "Evaluation of the ERA5 reanalysis precipitation dataset over Chinese Mainland," *J. Hydrol.*, vol. 595, Apr. 2021, Art. no. 125660.

[33] C. Yu, Z. Li, and N. T. Penna, "Interferometric synthetic aperture radar atmospheric correction using a GPS-based iterative tropospheric decomposition model," *Remote Sens. Environ.*, vol. 204, pp. 109–121, Jan. 2018.

[34] C. Yu, Z. Li, and N. T. Penna, "Triggered afterslip on the southern Hikurangi subduction interface following the 2016 Kaikōura earthquake from InSAR time series with atmospheric corrections," *Remote Sens. Environ.*, vol. 251, p. 17, Dec. 2020.

[35] C. Yu, Z. Li, N. T. Penna, and P. Crippa, "Generic atmospheric correction model for interferometric synthetic aperture radar observations," *J. Geophys. Res., Solid Earth*, vol. 123, no. 10, pp. 9202–9222, Oct. 2018.

[36] R. Xiao, C. Yu, Z. Li, and X. He, "Statistical assessment metrics for InSAR atmospheric correction: Applications to generic atmospheric correction online service for InSAR (GACOS) in eastern China," *Int. J. Appl. Earth Observ. Geoinformation*, vol. 96, Apr. 2021, Art. no. 102289.

[37] L. Zhao, R. Liang, X. Shi, K. Dai, J. Cheng, and J. Cao, "Detecting and analyzing the displacement of a small-magnitude earthquake cluster in Rong county, China by the GACOS based InSAR technology," *Remote Sens.*, vol. 13, no. 20, p. 4137, Oct. 2021.

[38] Y. Cao, S. Jónsson, and Z. Li, "Advanced InSAR tropospheric corrections from global atmospheric models that incorporate spatial stochastic properties of the troposphere," *J. Geophys. Res., Solid Earth*, vol. 126, no. 5, May 2021, Art. no. e2020JB020952.

[39] C. Yu, N. T. Penna, and Z. Li, "Optimizing global navigation satellite systems network real-time kinematic infrastructure for homogeneous positioning performance from the perspective of tropospheric effects," *Proc. Roy. Soc. A, Math., Phys. Eng. Sci.*, vol. 476, p. 2242, Oct. 2020.

[40] M. P. Uddin, M. A. Mamun, and M. A. Hossain, "PCA-based feature reduction for hyperspectral remote sensing image classification," *IETE Tech. Rev.*, vol. 38, no. 4, pp. 377–396, Jul. 2021.

[41] Y. Chen, Z. Lin, X. Zhao, G. Wang, and Y. Gu, "Deep learning-based classification of hyperspectral data," *IEEE J. Sel. Topics Appl. Earth Observ. Remote Sens.*, vol. 7, no. 6, pp. 2094–2107, Jun. 2014.

[42] H. Ghassemian, "A review of remote sensing image fusion methods," *Inf. Fusion*, vol. 32, pp. 75–89, Nov. 2016.

[43] I. T. Jolliffe, *Principal Component Analysis*. New York, NY, USA: Springer, 2006, pp. 1–21.

[44] P. Berardino, G. Fornaro, R. Lanari, and E. Sansosti, "A new algorithm for surface deformation monitoring based on small baseline differential SAR interferograms," *IEEE Trans. Geosci. Remote Sens.*, vol. 40, no. 11, pp. 2375–2383, Nov. 2002.

[45] A. Pepe and R. Lanari, "On the extension of the minimum cost flow algorithm for phase unwrapping of multitemporal differential SAR interferograms," *IEEE Trans. Geosci. Remote Sens.*, vol. 44, no. 9, pp. 2374–2383, Sep. 2006.

[46] A. Hooper and H. A. Zebker, "Phase unwrapping in three dimensions with application to InSAR time series," *J. Opt. Soc. Amer. A, Opt. Image Sci.*, vol. 24, no. 9, pp. 2737–2747, Aug. 2007.

[47] D. A. Schmidt and R. Bürgmann, "Time-dependent land uplift and subsidence in the Santa Clara Valley, California, from a large interferometric synthetic aperture radar data set," *J. Geophys. Res., Solid Earth*, vol. 108, no. B9, Sep. 2003.

[48] T. R. Lauknes, H. A. Zebker, and Y. Larsen, "InSAR deformation time series using an L_1-norm small-baseline approach," *IEEE Trans. Geosci. Remote Sens.*, vol. 49, no. 1, pp. 536–546, Jan. 2011.

[49] M. Manzo, Y. Fialko, F. Casu, A. Pepe, and R. Lanari, "A quantitative assessment of DInSAR measurements of interseismic deformation: The southern San Andreas Fault case study," *Pure Appl. Geophys.*, vol. 169, no. 8, pp. 1463–1482, Aug. 2012.

[50] W. C. Hammond, G. Blewitt, Z. Li, H.-P. Plag, and C. Kreemer, "Contemporary uplift of the Sierra Nevada, western United States, from GPS and InSAR measurements," *Geology*, vol. 40, no. 7, pp. 667–670, Jul. 2012.

[51] H. A. Zebker and J. Villasenor, "Decorrelation in interferometric radar echoes," *IEEE Trans. Geosci. Remote Sens.*, vol. 30, no. 5, pp. 950–959, 1992.

[52] C. Yu, N. T. Penna, and Z. Li, "Generation of real-time mode high-resolution water vapor fields from GPS observations," *J. Geophys. Res., Atmos.*, vol. 122, no. 3, pp. 2008–2025, Feb. 2017.

[53] C. Yu, Z. Li, and G. Blewitt, "Global comparisons of ERA5 and the operational HRES tropospheric delay and water vapor products with GPS and MODIS," *Earth Space Sci.*, vol. 8, no. 5, May 2021, Art. no. e2020EA001417.

[54] H. Hotelling, "Analysis of a complex of statistical variables into principal components," *J. Educ. Psychol.*, vol. 24, no. 6, pp. 417–441, Sep. 1933.

[55] V. Klema and A. Laub, "The singular value decomposition: Its computation and some applications," *IEEE Trans. Autom. Control*, vol. 25, no. 2, pp. 164–176, Apr. 1980.

[56] C. W. Chen and H. A. Zebker, "Phase unwrapping for large SAR interferograms: Statistical segmentation and generalized network models," *IEEE Trans. Geosci. Remote Sens.*, vol. 40, no. 8, pp. 1709–1719, Aug. 2002.

[57] J. Stockamp, "Establishing wide-scale mapping of vertical land motion with advanced DInSAR time series analysis in Scotland," Ph.D. dissertation, School Geographical Earth Sci. College Sci. Eng, University Glasgow, Scotland, U.K., 2018.

[58] K. W. Hudnut et al., "Continuous GPS observations of postseismic deformation following the 16 October 1999 Hector Mine, California, earthquake (Mw 7.1)," *Bull. Seismological Soc. Amer.*, vol. 92, no. 4, pp. 22–1403, May 2002.

[59] J. R. Murray, P. Segall, P. Cervelli, W. Prescott, and J. Svarc, "Inversion of GPS data for spatially variable slip-rate on the San Andreas Fault near Parkfield, CA," *Geophys. Res. Lett.*, vol. 28, no. 2, pp. 359–362, Jan. 2001.

[60] U. Wegmüller and C. Werner, "Gamma SAR processor and interferometry software," in *Proc. 3rd ERS Symp. Space Service Our Environ.*, Florence, Italy, 1997, pp. 1687–1692.

[61] T. J. Flynn, "Two-dimensional phase unwrapping with minimum weighted discontinuity," *J. Opt. Soc. Amer. A, Opt. Image Sci.*, vol. 14, no. 10, pp. 2692–2701, Oct. 1997.

[62] J. Xu, D. An, X. Huang, and P. Yi, "An efficient minimum-discontinuity phase-unwrapping method," *IEEE Geosci. Remote Sens. Lett.*, vol. 13, no. 5, pp. 666–670, May 2016.

[63] J. R. Murray and J. Svarc, "Global positioning system data collection, processing, and analysis conducted by the US Geological Survey Earthquake Hazards Program," *Seismological Res. Lett.*, vol. 88, no. 3, pp. 916–925, May 2017.

[64] G. W. Bawden, W. Thatcher, R. S. Stein, K. W. Hudnut, and G. Peltzer, "Tectonic contraction across Los Angeles after removal of groundwater pumping effects," *Nature*, vol. 412, no. 6849, pp. 812–815, Aug. 2001.

[65] E. Blackwell, M. Shirzaei, C. Ojha, and S. Werth, "Tracking California's sinking coast from space: Implications for relative sea-level rise," *Sci. Adv.*, vol. 6, no. 31, Jul. 2020, Art. no. eaba4551.

[66] Y. Fialko, M. Simons, and D. Agnew, "The complete (3-D) surface displacement field in the epicentral area of the 1999MW7.1 Hector Mine earthquake, California, from space geodetic observations," *Geophys. Res. Lett.*, vol. 28, no. 16, pp. 3063–3066, Aug. 2001.

Xuesong Zhang received the B.S. degree from Chang'an University, Xi'an, China, in 2019, where he is currently pursuing the Ph.D. degree with the College of Geological Engineering and Geomatics.

He is also a member of the Big Data Center for Geosciences and Satellites (BDCGS), Xi'an. His research focuses on synthetic aperture radar (SAR) and interferometric SAR (InSAR).

Zhenhong Li (Senior Member, IEEE) received the B.Eng. degree in geodesy from the Wuhan Technical University of Surveying and Mapping (currently Wuhan University), Wuhan, China, in 1997, and the Ph.D. degree in GPS, geodesy, and navigation from University College London, London, U.K., in 2005.

He is currently a Professor of imaging geodesy with the College of Geological Engineering and Geomatics, Chang'an University, Xi'an, China, the Vice Director of the Key Laboratory of Loess, Xi'an, and the Director of the Key Laboratory of Western China's Mineral Resource and Geological Engineering, Ministry of Education, Xi'an. He is also a Visiting Professor with the School of Engineering, Newcastle University, Newcastle upon Tyne, U.K. He is also a Principal Investigator of the Generic Atmospheric Correction Online Service (GACOS) for interferometric synthetic aperture radar. His research interests include space geodesy and remote sensing (mainly InSAR and GNSS) and their applications to geohazards (e.g., earthquakes, landslides, and land subsidence) and precision agriculture.

Dr. Li is a fellow of the International Association of Geodesy and an Associate Editor of *Advances in Space Research* and *Remote Sensing*.

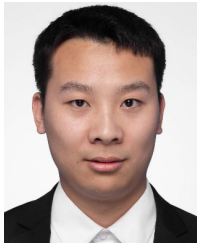

Zhenjiang Liu received the B.S. degree from the Institute of Disaster Prevention, Langfang, China, in 2020. He is currently pursuing the Ph.D. degree with the College of Geological Engineering and Geomatics, Chang'an University, Xi'an, China.

He is also a member of the Big Data Center for Geosciences and Satellites (BDCGS), Xi'an. His research focuses on seismic inversion using InSAR.